Biomimetic Carbon-Fiber Systems Engineering: A Modular Design Strategy to Generate Biofunctional Composites from Graphene and Carbon Nanofibers

Mohammadreza Taale[†], *Fabian Schütt*[‡], *Tian Carey*[§], *Janik Marx*[‖], *Yogendra Kumar Mishra*[‡], *Norbert Stock*[⊥], *Bodo Fiedler*[‖], *Felice Torrisi*[§], *Rainer Adelung*[‡], *Christine Selhuber-Unkel*[†]*.

[†]Biocompatible Nanomaterials, Institute for Materials Science, Kiel University, Kaiserstr. 2, D-24143 Kiel, Germany

[‡]Functional Nanomaterials, Institute for Materials Science, Kiel University, Kaiserstr. 2, D-24143 Kiel, Germany

[§]Cambridge Graphene Centre, University of Cambridge, 9 JJ Thomson Avenue, Cambridge CB3 0FA, UK

[‖]Institute of Polymer and Composites, Hamburg University of Technology, Denickestr. 15, D-21073 Hamburg, Germany.

[⊥]Institute of Inorganic Chemistry, Kiel University, Max-Eyth Straße 2, D-24118 Kiel, Germany.

Keywords: Tissue engineering, CNT, Graphene, Aerographite, ZnO, 3D scaffold, cell adhesion.

ABSTRACT

Carbon-based fibrous scaffolds are highly attractive for all biomaterial applications that require electrical conductivity. It is additionally advantageous if such materials resembled the structural and biochemical features of the natural extracellular environment. Here we show a novel modular design strategy to engineer biomimetic carbon-fiber based scaffolds. Highly porous ceramic zinc oxide (ZnO) microstructures serve as 3D sacrificial templates and are infiltrated with carbon nanotube (CNT) or graphene dispersions. Once the CNTs and graphene uniformly coat the ZnO template, the ZnO is either removed by hydrolysis or converted into carbon by chemical vapor deposition (CVD). The resulting 3D carbon scaffolds are both hierarchically ordered and free-standing. The properties of the micro-fibrous scaffolds were tailored with a high porosity (up to 93 %), high Young's modulus (~0.027 to ~22 MPa), and an electrical conductivity of (~0.1 to ~330 S/m), as well as different surface compositions. Cell viability and fibroblast proliferation rate and protein adsorption rate assays have shown that the generated scaffolds are biocompatible and have a high protein adsorption capacity (up to 77.32 ±6.95 mg/cm^3), so that they not only are able to resemble the ECM structurally, but also biochemically. The scaffolds also allow for the successful growth and adhesion of fibroblast cells showing that we provide a novel, highly scalable modular design strategy to generate biocompatible carbon-fiber systems that mimic the extracellular matrix with the additional feature of conductivity.

1. INTRODUCTION

Regenerative medicine aims at developing microenvironments for the regrowth of damaged or dysfunctional tissue and organs. New promising strategies of regenerative medicine make use of biomaterial scaffolds that resemble the chemical composition,[1] the topographical structure, and the 3D micro- and nanoenvironment of ECM[2]. The ECM consists of interwoven protein fibers, such as collagens, in different ranges of diameters varying from a few (<5 nm) up to several hundred nm for bundled collagen fibrils.[3] The chemical, structural and mechanical features of the ECM significantly control cell migration, as well as tissue development and maintenance,[4] so that finding novel ways to mimic the ECM is a highly important task in biomaterials science. As the diameter (< 5 nm) and length (< 500 nm) of unbundled collagen fibrils are in the range of those of CNTs,[3] CNTs present an interesting substitute for collagen fibrils.

A general goal of artificially fabricated biomaterial scaffolds is to promote cells to differentiate and proliferate in three dimensions so that they fulfill their functions in the artificial tissue and integrate well after implantation.[5] Particularly the microstructure and porosity of a scaffold are key to spatially organized cell growth, besides the induction of specific biological functions in the regenerated tissue. Adjustment of pore size, shape and interconnectivity of a scaffold ensure that cell migration, as well as oxygen and nutrient contribution are similar to the conditions in natural tissue.[6] Often, a large pore size in the range of a few micrometers supports cell migration and ensures the transport of nutrition and waste products.[7]

In neural implants and heart tissue engineering the electrical conductivity of a scaffold material is often a further requirement necessary for cellular signaling and function.[8] For example, conductivities of 0.03–0.6 S/m have been reported for cardiac muscles.[9] Carbon-based nanomaterials can in principle fulfill such requirements for 3D assemblies.[10,11] CNTs have a high

electrical conductivity (up to 67000 S/cm)[12] and chemical stability (e.g. against acids)[13]; graphene can have high surface areas (2630 m^2/g)[14] and high electrical conductivity ($10^7 – 10^8$ S/m)[15]. CNTs and graphene both have attracted significant attention in biomedical applications, ranging from bio-sensors[16], drug and gene delivery[17], to targeted bio-imaging[17]. In addition, compared to other carbon-based nanomaterials the high physical aspect ratio of CNTs (up to 3750 length/diameter) and graphene provides a sufficient surface area for the attachment of adhesion ligands and cells.[14,18] Regarding neural tissue engineering, 3D graphene foams[19] and graphene films[18] have been proven to enhance neural stem cell differentiation towards astrocytes and neurons.[20]

An important requirement for such carbon-containing scaffolds is biocompatibility. The biocompatibility of CNTs depends on the concentration of CNTs[21], their degree of purification, the synthesis method[22], aspect ratio plus the diameter and the number of CNTs walls[23], as well as on their surface functionalization.[24] Although many studies have proven the feasibility of CNTs as biocompatible materials,[25] the cytotoxicity of CNTs is still a concern due to residual metal catalysts, amorphous carbon and CNT aggregation that can occur within the cell.[26] In contrast, graphene has been reported to be biocompatible and is readily applicable for a variety of biological applications, including the use of neuronal cells[18], cardiomyocytes[27], and osteoblasts[28] cells. Graphene oxide is an interesting graphene derivative, as it consists of a single atomic layer and hydrophilic functional groups such as carboxylic acid, hydroxyl and epoxide.[29] In particular, it has been demonstrated that graphene oxide has a strong tendency to interact with peptides and proteins via physical or chemical bonds.[30] Therefore, graphene and graphene oxide have great potential in biomedical applications as they can easily be converted into biofunctional, peptide- or protein-coated surfaces. Moreover, carbon microtube materials, specifically aerographite

(AG), are of further interest as biomaterials due to their electrical conductivity (0.2 up to 0.8 S/m)[31] and their highly porous (up to 99.99 %)[32] 3D interconnected network. A recent study has demonstrated the feasibility of AG as a suitable 3D matrix for cell migration and proliferation.[33] However, a clear pathway to generate a highly porous biocompatible ECM mimetic scaffold with tunable porosity, electrical conductivity, and suitable mechanics for biomedical applications has so far been missing.

To solve this challenge, we demonstrate a novel modular design strategy to generate hierarchically structured carbon-based, micro-fibrous scaffold materials with adjustable electrical and mechanical properties that mimic the structure of the extracellular matrix. The materials investigated here are biocompatible, support cell proliferation and adhesion, and open the gateway to future biomaterial development, where biocompatibility and electrical conductivity are vital for cell proliferation and stimulation.

2. RESULTS AND DISCUSSION

2.1. Novel types of graphitic scaffolds by CNT and graphene infiltration

Different types of fibrous 3D carbon scaffolds have been prepared based on our modular template-mediated method. Figure 1 shows the modular design strategy of our fabrication method. The fabrication is based on using pre-sintered highly porous (porosity >93 %) ceramic ZnO templates as sacrificial material.[32] These ZnO templates themselves consist of interconnected tetrapod-shaped ZnO particles. Representative scanning electron microscopy (SEM) images of the ZnO templates are shown in Supplementary Figure S2. The highly porous ZnO templates have an interstitial space of approximately 10 µm to 100 µm between filaments, which in turn have diameters between 0.5 and 5 µm. Therefore, the spatial geometry and organization of the microtube-shaped structures of the ZnO template is comparable to that of the ECM.[34]

For coating the ZnO templates with carbon nanomaterials (e.g CNTs, Graphene), a simple infiltration process is used to infiltrate the entire 3D template with a CNT dispersion as described by Schütt et. al[35]. In addition, here we demonstrate the feasibility of this technique is also for graphene dispersions. The infiltration process relies on the superhydrophilicity of the ZnO template[36] that is a direct result of the combination of the hydrophilic character of the individual tetrapodal-shaped ZnO microparticles and the high porosity (>93 %) of the template. During water evaporation the nanomaterials form a widely homogenous coverage[35] around the ZnO microrods (Supporting Information, Figures S3,S4). The amount of CNTs and graphene flakes covering the ZnO template can be controlled by cyclically repeating the infiltration process several times (Supporting Information, Figures S3, S4). SEM images revealed that the infiltrated

CNTs form a layer made of self-entangled CNTs around the ZnO network (Supporting Information, Figure S4). Similarly to CNTs, graphene flakes in dispersion also form a homogeneous layer around the ZnO (Supporting Information, Figure S3).

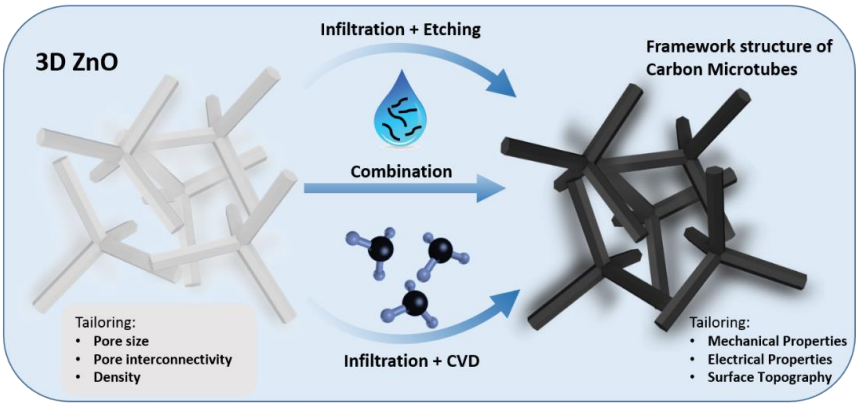

Figure 1. Schematic illustration of the different 3D carbon tube structures: The highly porous ZnO template can be either infiltrated with a nanoparticle dispersion (e.g. graphene, CNT) leading to a homogenous coating around the tetrapodal particles or, the template can be converted to a graphitic structure using a CVD process (aerographite). The combination of both processes leads to a modular design strategy, especially in terms of conductivity, mechanical stiffness and surface topography.

To generate free-standing scaffolds from the ZnO templates after coating them with carbon nanomaterials, the ZnO must be carefully removed. We have used three different processes to remove the sacrificial ZnO network after infiltration (Figure 1): i) hydrolyzing the sacrificial ZnO template by a HCl solution[35] (Supporting Information, Figure S5a), ii) converting the ZnO template via a CVD process[31] (Supporting Information, Figure S5b,c), iii) using a carbothermal reduction process[37] in combination with glucose as a carbon source. Each of these processes leads to a specific type of carbon-based scaffold. Therefore, the results of these processes (Supporting Information, Figure S5) are discussed in the following sections.

2.2. Free-standing carbon nanotube networks (CNTT) scaffolds from hydrolysis of the sacrificial ZnO template by HCl

When HCl is used to dissolve the ZnO in CNT-coated ZnO templates, hierarchically structured CNTT scaffolds are formed. These structures consist of interconnected hollow tubes, which are composed of self-entangled CNTs networks, as reported previously[35]. SEM images of the resulting CNTT scaffolds are presented in Figure 2a-c. The presented structures demonstrate a hierarchical architecture, as the scaffolds are porous, being composed of micro-tetrapods (Figure 2a,b), which in turn consist of nanoscale CNTs (Figure 2c). The HCl-based ZnO dissolution can only be applied for templates infiltrated with CNTs. Templates infiltrated with graphene only led to collapsing structures (data not shown), presumably as the graphene flakes cannot interweave.

2.3. ZnO conversion to AG via CVD forms composites with embedded nanoparticles

We also use a CVD process to remove the ZnO, resulting in a thin (~15 nm) film of graphite around the entire template similar to the graphitic shells in AG[31]. The CVD process can be applied if the ZnO is coated with either CNTs or graphene (Supporting Figure S6). Then, the AG serves as an additional backbone. This is the case in all of our CVD-based scaffolds, i.e. in composites of graphene and aerographite (AG-G) and in composites of multi-walled CNTs and aerographite (AG-CNTT) (Figure 2 d-l). The modular design of the fabrication process allows us to change and tailor the surface topography of the hollow graphitic micro-tubes. Up to 5 µm long CNTs are formed perpendicular to the surface of micro-tubes on AG-G and AG-CNTT during the CVD process (Figure 2f). Such CNTs are not formed on pure AG (Figure 2i). The growth of new carbon nanotubes on AG-G networks (Figure 2l, red arrows) is most likely attributed to the

adsorption of carbon atom clusters on the active sites of the graphene surface during the CVD process[38].

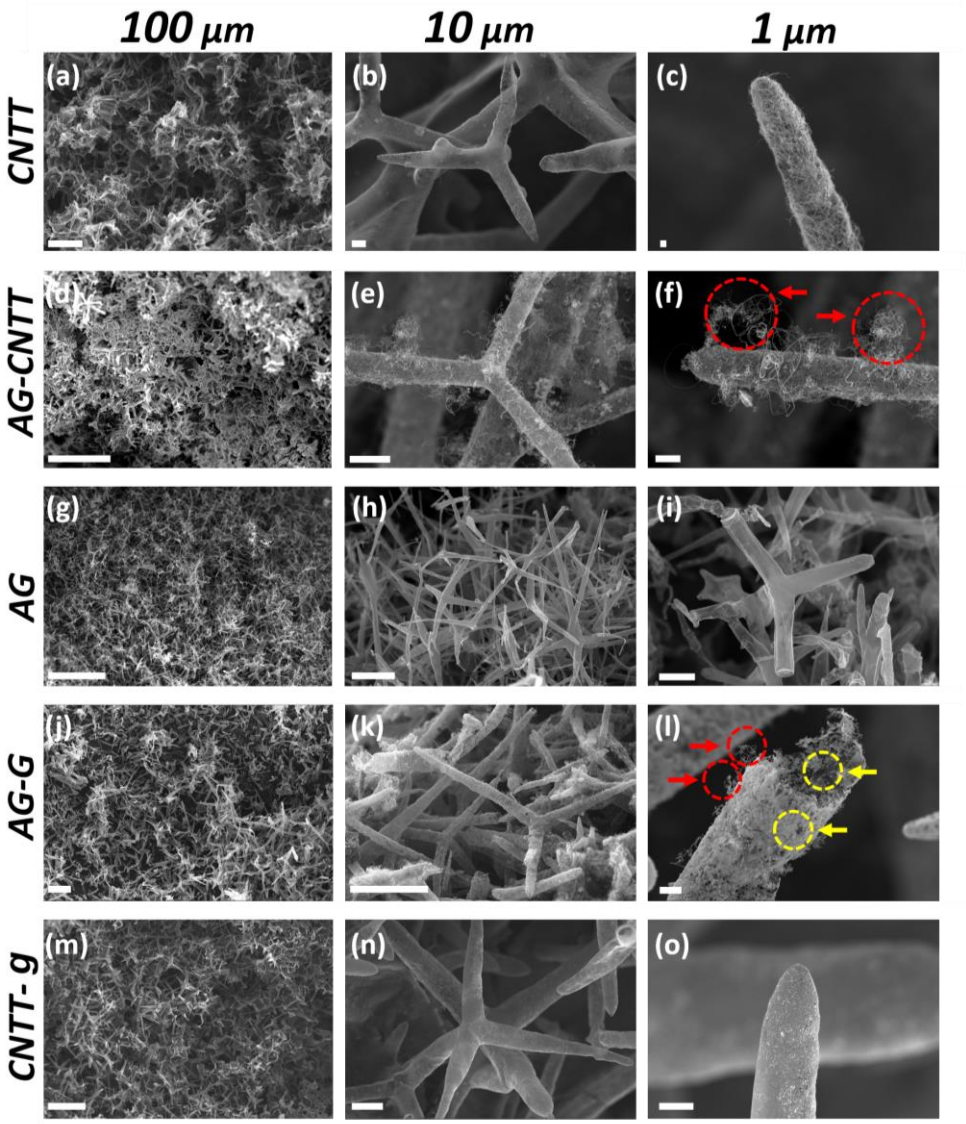

Figure 2. SEM images from low to high magnification of the different 3D carbon structures. a-c) Aerographite (AG), d-f) Aerographite with incorporated graphene (AG-G), yellow arrows point at nanopores on the surface of aerographite, g-i) Carbon nanotube tubes (CNTT), j-l) Aerographite with incorporated CNTs (AG-CNTT), red arrows show the grown CNTs during the CVD procedure, and m-o) Carbon nanotube tubes incorporated into a thick carbon layer (CNTT-g).

2.4. A carbothermal reduction process leads to novel types of graphitic structures with embedded CNTs

In the carbothermal reduction reaction[37], glucose acts as the carbon source enabling the reduction of ZnO in a quartz tube furnace at 950°C under argon atmosphere. To do so, ZnO templates were infiltrated with a mixture of glucose and CNTs. The carbothermal reduction of ZnO to Zn(g)[37] leads to ZnO removal and to the formation of graphitic shells, thus resulting in the so-called CNTT-g structure (Figure 2m-o). We have confirmed the removal of ZnO by Raman spectroscopy (Figure 3, CNTT-g graph) (see next paragraph). Furthermore, this process results in a scaffold with a microstructure that is comparable to that of the AG-CNTT scaffold (Figure 2 e,n). However, the graphitic shells of the CNTT-g scaffold appear to be thicker than those of the AG-CNTT scaffold (Figure 2 n,o). Additionally, in contrast to the AG-CNTT structures no additional CNTs are grown (Figure 2n) in the CNTT-g case.

Figure 3 shows Raman spectra (Renishaw 1000 InVia) of all the carbon-based structures. Raman spectroscopy is used to examine the structural fingerprint of each material at a wavelength of 514.5 nm with an incident power of ~0.1 mW. The graphene and CNT inks were drop cast onto Si/SiO_2 substrates before measurement. For the graphene ink (red curve), the G peak (~1586) corresponds to the E_{2g} phonon at the Brillouin zone center, the D peak located at ~1350 cm^{-1} corresponds to the breathing modes of the sp^2 carbon atoms and requires a defect for its activation[39]. Typically, graphene inks are produced by liquid phase exfoliation, therefore we attribute this peak to edge defects rather than to defects in the basal plane[40]. The 2D peak located at ~2700 cm^{-1} is the D peak overtone and can be fitted by a single Lorentzian indicating electronically decoupled graphene monolayers[41].

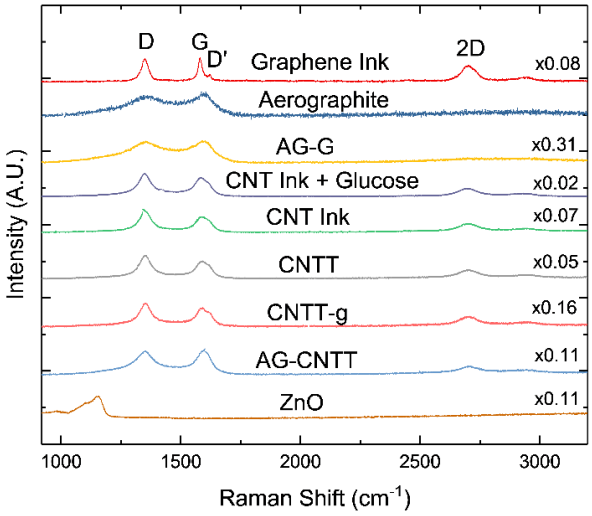

Figure 3. Raman spectroscopy of aerographite, ZnO, CNTT, AG-CNTT, CNTT-g, AG-G, graphene and CNT inks.

The aerographite (dark blue curve) shows a G peak position Pos(G) ~1600 cm^{-1} and the absence of a distinct 2D peak, indicating the more defective nature this sample and a lack of structural order in the aerographite[42]. The AG-G (yellow curve) structure has a similar spectrum to that of aerographite with a D and G peak located at ~1350 cm^{-1} and ~1600 cm^{-1} respectively, indicating that the material is mostly composed of aerographite and graphene, given the selective etching of the ZnO scaffold during the CVD reduction[31]. The spectra of the CNT ink (green curve) and CNT ink with glucose (purple curve) show a D peak at ~1350 cm^{-1}, a G peak at ~1580 cm^{-1}, and a 2D peak at ~2700 cm^{-1}. The peaks from the glucose residue are too weak to be observed. Consequently, the CNTT spectra (gray curve), AG-CNTT (blue curve) and CNTT-g (pink curve) have D, G and 2D peaks that demonstrate the presence of the CNTs. The ZnO spectra (brown curve) displays several peaks below 1200 cm^{-1}, predominately created from the intense peak at 1158 cm^{-1} attributed to the $2A_1(LO)$ and $2E_1(LO)$ mode at the Brillouin zone center[43]. However, no peaks attributed to ZnO are observed in any of the CNTT or aerographite scaffolds, proving the complete removal of the ZnO template.

2.5. Scaffold mechanics can be tailored over several orders of magnitudes

Figure 4 shows the Young's moduli and electrical conductivities of CNTT, AG-CNTT, CNTT-g, AG and AG-G. The scaffold with the lowest stiffness is AG with a Young's modulus of 16 kPa, which is comparable to previously reported values[31]. AG-G has a Young's modulus of up to 27 kPa, thus adding graphene into the graphitic shells of AG results in a mechanical reinforcement of the scaffold (~170 %). This reinforcement is in a similar range as that of other graphene-reinforced porous networks, e.g. graphene/chitosan composites[44] (~200 %). In contrast to AG-G, AG-CNTT scaffolds are much stiffer (Figure 4), with a Young's modulus reaching ~22 MPa.

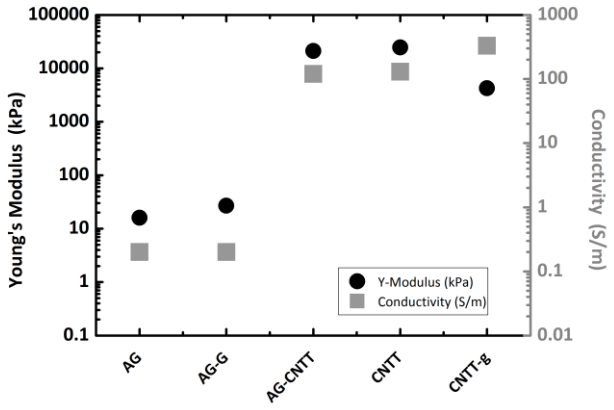

Figure 4. Young's modulus (measured under compression) and electrical conductivity of the 3D CNTT, AG-CNTT, CNTT-g and AG-G scaffolds. All structures containing CNTs have a higher Young's modulus and conductivity compared to those without CNTs. The values for pure AG and CNTTs were taken from the corresponding publications[31,35], whereas the other values were measured using a self-built electro-mechanical testing setup.

This reinforcement by a factor of about 1000 is presumably due to the reinforcement of CNTs on the nanoscale by self-entanglement[35]. Hence, the mechanical reinforcement of AG by CNTs is higher than in other CNT-reinforced porous biomaterials, including gelatin methacrylate

(GelMA)-CNT composites[45] and poly(propylenefumarate)-CNT composites[46]. The Young's modulus of CNTT-g (~ 4 MPa) is in between the moduli of AG-G and AG-CNTT. These results confirm that the incorporation of CNTs and graphene into 3D scaffolds compensates for the typically low mechanical Young's moduli of porous structures[47] and that AG provides a stable backbone for CNTT scaffolds. In addition, structural integrity of AG-G scaffold is demonstrated during a long-cycle compression test (Figure S7) (Supporting information, Video S1).

2.6. Tailoring scaffold conductivity

We also investigated the electrical properties of our scaffolds (Figure 4, grey squares). AG-G and AG have similar electrical conductivities of around 0.5 S/m and 0.2 S/m, whereas the conductivity of AG-CNTT and CNTT-g are about 120 S/m and 130 S/m (Figure 4). Hence, AG-CNTT and CNTT-g clearly have higher electrical conductivities than CNT-containing electrospun fibrous composites (3.5 S/m)[48], which are applied in cardiac tissue engineering. The increase in conductivity of the scaffolds can be mainly attributed to the high conductivity of CNTs that are embedded in the graphitic shells of AG. This effect is more pronounced in the case of AG-CNTT and CNTT-g, presumably as a result of the conductive pathways formed by the self-entangled CNT networks. It has already been shown that by adjusting the CNT concentration during the infiltration process the conductivity of CNTT can be tailored between 10^{-6} to 130 S/m[35]. Indeed, CNTT-g has the highest conductivity (330 S/m) of our scaffolds.

2.7. Scaffolds strongly adsorb proteins

Albumin is an adhesive protein in plasma and can non-specifically bind to low-dimensional carbon-based materials via electrostatic interactions[49]. Therefore, we checked the albumin

adsorption capacity of the scaffolds using the bicinchoninic acid (BCA) assay. As shown in Figure 5, within the first 48 hours albumin adsorption is smaller on AG-G than on AG-CNTT, whereas its adsorption is very similar on all scaffolds later on. The highest protein absolute protein adsorption mass (30.23-22.6 ±2.76 mg/cm^3) was detected during the two first days of incubation, and the adsorption amount reduced to approximately two-thirds (23-69-20.64 ±2.39 mg/cm^3) during the third to fourth day of incubation. Overall, protein adsorption is very similar on all tested scaffolds, although CNTT, CNTT-g and AG-CNTT scaffolds adsorb a slightly higher protein amount (CNTT-g: 77.32±6.95 mg/cm^3, CNTT: 70.77 ±5.33 mg/cm^3, AG-CNTT: 68.08 ±6.73 mg/cm^3) than AG-G (64.92 ±7.2 mg/cm^3) (Figure 5a). This might be attributed to a higher protein adsorption capacity of CNTs than graphene flakes due to van der Waals forces and electrostatic interactions[30].

To compare our results of protein adsorption with other studies, we needed to relate them to the weight of the scaffolds by taking into account their density (Table 1). Figure 5b shows that protein adsorption per weight of CNTT, CNTT-g and AG-CNTT scaffolds is different for the different scaffold types (CNTT-g: 147.9 ±13.42 mg/g, CNTT: 128.9 ±9.69 mg/g, AG-CNTT: 115.14 ±11.38 mg/g). It is also higher than on single-walled CNTs and graphene (~ 100 mg/g)[30] and on nano-porous Silica (~ 70 mg/g)[50]. In addition, due its low density, AG-G adsorbs even more protein per weight (1512.25 mg/g) after 144 hours, e.g. about ten times more than our other scaffolds. The albumin adsorption on AG-G even after 48 hours (527 mg/g) is comparable to that of graphene oxide (~ 500 mg/g)[30].

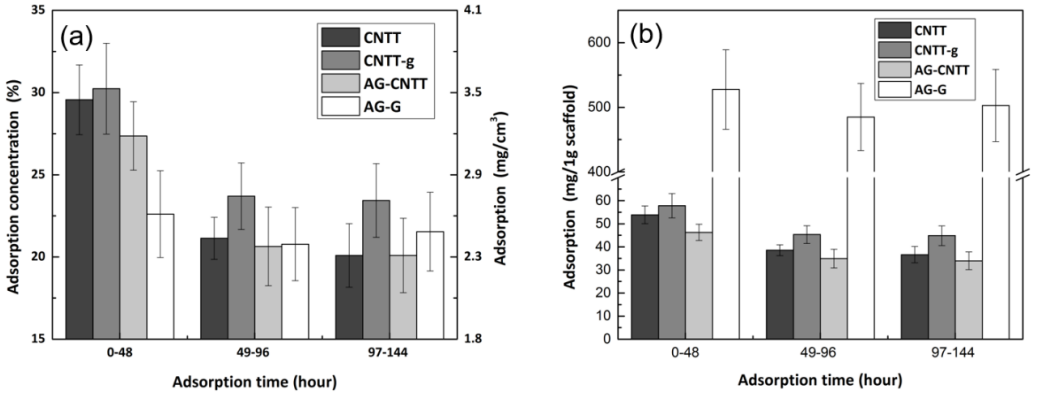

Figure 5. Protein adsorption on CNTT, AG-CNTT, CNTT-g and AG-G during 0-48, 49-96 and 97-144 hours of incubation with albumin solution (1mg/ml). a) Absolute protein adsorption amount per scaffold volume. b) Absolute protein adsorption amount per scaffold weight.

Table 1. Full names and abbreviations of fabricated materials and scaffolds in our study.

Full name	**Abbreviation**	**Density (g cm^{-3})**	**Porosity (%)**
Zinc Oxide	**ZnO**	**-**	**-**
Multi-walled carbon nanotube	**MWCNT**	**-**	**-**
Aerographite	**AG**	**~ 200*10^{-6}** [31]	**Up to ~ 99.9** [31]
Carbon nanotube tube	**CNTT**	**~ 0.064**	**~ 94**
Carbon nanotube tube - glucose	**CNTT-g**	**~ 0.061**	**~ 90**
Aerographite – carbon nanotube tube	**AG-CNTT**	**~ 0.069**	**~ 95**
Aerographite – graphene	**AG-G**	**~ 0.005**	**~ 96**

2.8. Biocompatibility of the carbon-based scaffolds

Biocompatibility of the scaffolds is investigated by Methylthiazolyldiphenyl-tetrazolium bromide metabolic activity (MTT) and WST-1 assays, as well as by proliferation studies. Figure 6 shows the results for CNTT, CNTT-g, AG-CNTT and AG-G samples using an MTT assay, demonstrating that all scaffolds are biocompatible, hosting a similar number of viable cells as the negative control. As cell adhesion is not possible on pristine AG without functionalization[33], biocompatibility of AG is not investigated again in this study.

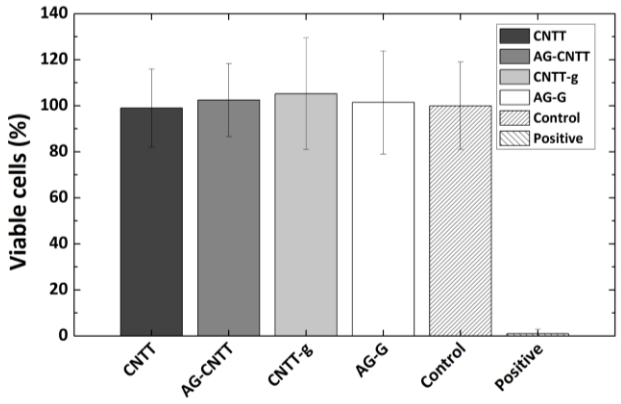

Figure 6. Percentage of viable cells (REF52wt) relative to the negative control, as determined in an MTT assay (four independent experiments, five technical repeats in each of them). Error bars denote standard deviation.

Figure 7 shows the proliferation rate of rat embryonic fibroblast cells (REF52 wt) cultured on CNTT, CNTT-g, AG-CNTT and AG-G samples relative to cells cultured on a culture dish. CNT-containing scaffolds (CNTT, CNTT-g and AG-CNTT) lead to higher proliferation rates (~300 % up to 320 %) than graphene-containing structures (AG-G) (~240 %) after 7 days in culture. As fibroblast proliferation depends on matrix stiffness[51] an increase in stiffness might also lead to an increase in fibroblast proliferation[52], this can be attributed to translation of mechanical cues from

the matrix into a biochemical one via mechanosensory receptors such as focal adhesions[53]. Specifically, it has been reported that fibroblasts need substrates with a minimum Young's modulus of 20-30 kPa to spread and 2 MPa to spread and polarize perfectly[51]. Hence, the huge difference in the Young's moduli of CNT-reinforced scaffolds (between 4 MPa in CNTT-g and 23 MPa in CNTT) and graphene-reinforced scaffolds (27 kPa in AG-G), can explain the higher proliferation rate of fibroblast cells on CNTT, AG-CNTT and CNTT-g compared to AG-G.

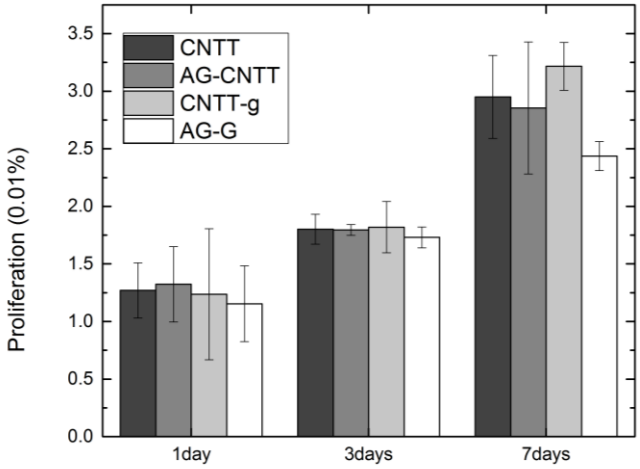

Figure 7. Results of WST-1 metabolic tests of cell proliferation rate (REF52wt). Mean values were determined from four independent experiments, each including five technical repeats. Error bars denote standard deviation and the raw data were normalized to the control and a correction factor was applied to account for unspecific adsorption (see Materials and Methods).

2.9. Carbon-based scaffolds as porous structures for cell growth

Fibroblast cells (REF52wt) were cultured for 7 days on the scaffolds to investigate cellular growth at the surface and inside. SEM images of critically point-dried cells (Figure 8) revealed that cells (highlighted in green) are attached to the surface of the scaffolds. Fibroblasts do not migrate strongly within a 3D network[54] but proliferate, so that we typically observe

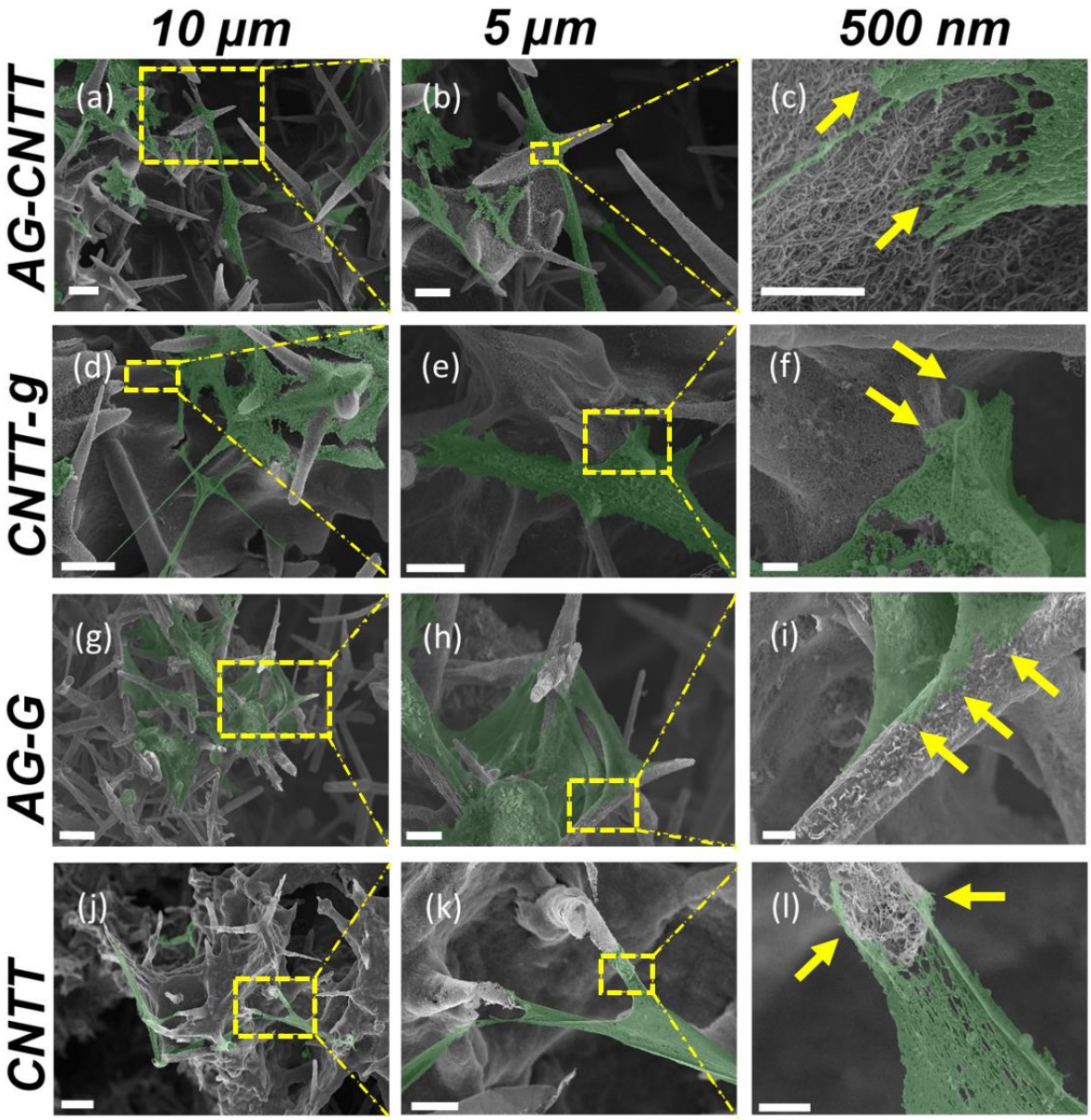

Figure 8. SEM images of REF52wt cells after 7 days of culturing within (a-c) AG-CNTT, (d-e) CNTT-g (g-i) AG-G (j-l) CNTT scaffolds, Left: medium sized overview images illustrate the growth of cells between the fibers in different directions and planes, Middle: zoomed-in images show well stretched cells along the fibers and their elongation, Right: close-up images on the adhesion sites proving the presence of strong contacts between the materials and the cell membrane (yellow arrows).

several cells at one location. Cells are sprawled and elongated between the filaments of scaffolds, and have a polygonal shape on all four scaffold types. Close-up images on the adhesion sites reveal tightly anchored membranes of cells to CNTs and graphene on the surface of structures, comparable to fibroblasts on AG functionalized with cyclic RGD peptides[33].

To investigate cell adhesion at the molecular level, we studied the presence of paxillin in adhesion structures. Paxillin is a component of focal adhesion clusters[55], therefore it can be assumed that more paxillin in contact with our scaffolds is related to stronger cell adhesion. We used cells that were stably transfected with yellow fluorescent protein (YFP)-paxillin and imaged the paxillin in fluorescence microscopy. Imaging fluorescence in 3D matrices compared to 2D is challenging[56]. Due to the low intensity of paxillin in the cells and the high light absorbance of our scaffolds[31], imaging the paxillin adhesions sites was only possible by using long acquisition times (5 sec), which resulted in background signals. Nevertheless, paxillin-containing adhesion sites can be distinguished around the filaments of the scaffolds. Based on the fluorescence images (Figure 9a-d, Figure S8), more adhesion clusters can be detected on CNT-reinforced scaffolds than on graphene-reinforced scaffolds. This could again result from the different mechanical properties of the scaffolds, but it is also in agreement with cell studies on multi-walled CNTs showing that NIH-3T3 fibroblasts form larger adhesion clusters on CNTs than on graphene[57].

A further important contribution to cell adhesion is the cytoskeleton, where networks of actin fibers determine cell shape and cell movements.[58] To investigate cellular actin networks on our scaffolds we investigated the fluorescence of phalloidin to detect actin fibers. Again, imaging deeply inside the scaffolds was impaired by the strong light absorbance of CNTs and graphene restricting it to the first 300 µm from surface. As shown in Figure 9, well-developed actin fibers

(in red) are indeed present within the fibroblasts. Furthermore, the cells are polarized and have oriented actin bundles. Figure 9a-c also shows that actin fibers on CNT-reinforced scaffolds (CNTT, AG-CNTT and CNTT-g) are mainly oriented in the direction of fibroblast protrusions (Figure 9a-c). Although many actin fibers can be detected in cells grown on AG-G (Figure 9d), they are neither well polarized nor elongated like the actin fibers in the cells on CNT-reinforced scaffolds (CNTT, AG-CNTT, CNTT-g). These results could again originate from the mechanical properties of our materials, similarly to proliferation rate and paxillin clusters.

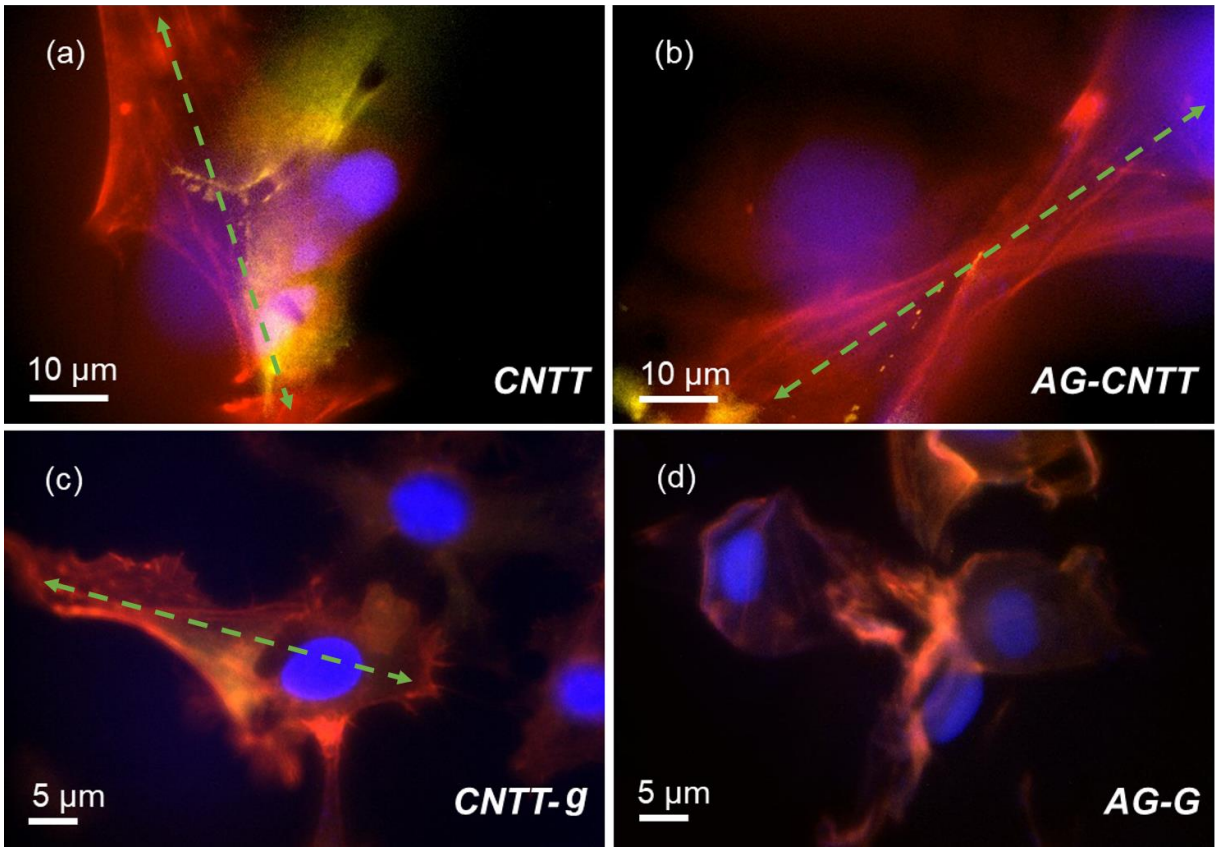

Figure 9. High magnification fluorescent images of REF52 YFP-paxillin cells on 3D scaffolds a) CNTT, b) AG-CNTT, c) CNTT-g, d) AG-G. YFP-paxillin is mainly distributed in small clusters (YFP; yellow), the nucleus was stained with Hoechst (DAPI; blue) and actin fibers were visualized by phalloidin (red). Fluorescent imaging took place in optical sections approximately between 50 and100 µm from the surface of the material. Adhesion sites are detectable (a, b) as

tiny yellow spots mainly around the tube-shaped filaments of CNTT and AG-CNTT structures. Due to the low intensity and small size of YFP-Paxillin (c, d), they are not clearly observed, which is also obscured by red (actin fibers) and blue (nucleus) channels in multichannel images. Green dashed-arrows illustrate the protrusion direction of the cells.

2.10. ECM-mimetic scaffolds

The open porous structure of our scaffolds with large free-volumes (> 95 %) should be highly beneficial for the growth and migration of cells, as the open pores allow the cells to freely migrate and proliferate within the scaffolds.[2] Moreover, in contrast to other studies on 3D porous structures, in which the alignment of CNTs[24] or graphene sheets[59] confined the accessibility of cavities, our carbon framework structures provide accessible interconnected pores from all sides (Figure 2). In addition, the hierarchical organization of structural elements, specifically self-entangled CNTs in the form of microtubes, is reminiscent of the hierarchical nano- and microstructure of the ECM. It should therefore in principle be possible to employ our modular design strategy to generate different composition-dependent structural and mechanical features similar to collagen[60] in ECM. As our scaffolds strongly adsorb proteins, it should also be possible to adsorb adhesion ligands typically present in ECM proteins, such as RGD[61]. In this way the scaffolds can be modified such that they finally mimic the ECM structurally and biochemically, but with the additional feature of conductivity.

3. CONCLUSIONS

In summary, we have introduced a novel modular design strategy to produce carbon-based scaffolds that mimic the ECM and allow for 3D cell growth. Biocompatibility studies revealed a high proliferation rate of fibroblasts as well as the ability of fibroblasts to develop paxillin-containing adhesion sites. In addition, the cells sprawl and elongate between single filaments of the scaffolds. Tuning electrical conductivity (~0.1 to ~330 S/m), stiffness (~10^{-3} to ~0.7 MPa), protein adsorption and porosity (up to ~99 %) of the scaffold provides great possibilities for culturing cells. Based on the proven protein adsorption capacity of the scaffolds, they are suitable for biofunctionalization and addition of other biochemical cues. This is particularly relevant in tissue engineering of electrically excitable tissue, e.g. heart tissue, as our scaffolds have tunable electrical conductivity. In addition, the fabrication procedure is very simple and can in principle be adopted to develop 3D assemblies from other low-dimensional nanomaterials (e.g. bioactive ceramic nanoparticles, polymeric nanofibers) by only changing the nanoparticle dispersion, as long as the nanoparticles are connected via strong physical contacts such as entanglement, fusion or physical locks. This makes the scaffolds promising candidates as conductive ECM-mimetic materials in many applications from regenerative medicine to 3D cell culture.

4. MATERIALS AND METHODS

4.1. Fabrication of 3D carbon scaffold materials

Templates of tetrapod shaped ZnO were fabricated by a previously developed flame transport synthesis method[32]. The resulting loose powder was pressed into a cylindrical shape (h = 3 mm, d = 6 mm) at a density of 0.3 g/cm³. The pellets were subsequently sintered for 5h at 1150°C to obtain an interconnected 3D ZnO network.[32] This structure is the sacrificial template used for fabrication of carbon-based scaffolds, i.e. free-standing CNTT, AG-CNTT and AG-G.

For the fabrication of the CNTT scaffolds the porous ZnO templates were infiltrated with an aqueous dispersion of multi-walled CNTs (1 wt %, CarboByk 9810, BYK Additives & Instruments) using a self-built computer-controlled syringe. The length of the CNTs can be on the order of a few micrometers, with diameters in the range of 20 to 60 nm[34]. After infiltration of ~90 µl of the CNT solution the samples were dried under ambient conditions for at least one hour. The process was repeated six times so that CNTs covered the ZnO template. Then, the ZnO backbone was removed by immersing the composite in a 1 M HCl solution overnight. The HCl solution was replaced by washing with pure ethanol (5 times washing). Finally, the etched structures were dried in a critical point dryer (EMS 3000) by using the automatic mode. The purge time was set to 15 minutes to ensure all ethanol was washed out, leaving free-standing CNTT[3].

To alter the CNTT structures further we added glucose (1 wt %) to the CNT ink used for infiltration. The infiltration into a ZnO template was then repeated four times. After that the samples were transferred into a quartz-tube furnace and heated to 950 °C under argon

atmosphere for 2 hours. During this process, the ZnO was removed by carbothermal reduction[45], leading to CNTT-g, which both contains the remnants of the glucose and embedded CNTs.

For the synthesis of AG-CNTT scaffolds, the CNT coated ZnO templates were exposed to a CVD process, as reported previously[31]. Briefly, the ZnO template was replicated into aerographite at ~760°C under a hydrogen and argon atmosphere in the presence of toluene as the source of carbon.[62] Thereby the CNTs were embedded into the graphite micro-tubes of aerographite while the ZnO was simultaneously etched by H_2.

A similar process was used to generate composites of graphene and aerographite (AG-G). The graphene ink was made by dispersing graphite flakes (12 mg/ml, Sigma-Aldrich No. 332461) and Triton-X-100 stabilization agent (1.7 mg/ml) in deionized water, followed by sonication (Fisherbrand FB15069, Max power 800 W) for 9 h.[63,64] The dispersion was then centrifuged (Sorvall WX100 mounting a TH-641 swinging bucket rotor) at 5k rpm for 1 hour to remove the thick flakes. The supernatant (i.e. the top 70 %) of the dispersion was then decanted to produce the final graphene ink. In supplementary Figure S1, optical absorption spectroscopy (Cary 7000) is used to estimate the flake concentration[65]. The flake concentration in the graphene ink is obtained via the Beer-Lambert law, which links the absorbance $A = \alpha c l$, with the beam path length l [m], the flake concentration c [g/L], and the absorption coefficient α [L/g m]. The graphene ink was diluted 1:20 with water/triton-x-100. An absorption coefficient of $\alpha \sim 1390$ L/ g m for the graphene ink at 660nm was utilized[66] estimating a graphene flake concentration of ~0.09 mg/ml, consistent with previous reports of graphene based inks[40,67]. The spectrum of the graphene ink is mostly featureless due to the linear dispersion of the Dirac electrons, while the peak in the UV region is a signature of the van Hove singularity in the graphene density of states[68]. The ZnO scaffold was infiltrated 50 times to achieve coverage of graphene around the

ZnO tetrapods, due to the low concentration of the ink (0.09 mg/ml). After infiltration, the CVD process (see process specification above) was used, to embed the graphene flakes into aerographite micro-tubes and to remove the ZnO template.

4.2. Mechanical and electrical characterization of 3D carbon scaffold materials

Mechanical and electrical characterization was performed using a self-built setup consisting of a Maerzhaeuser Wetzlar HS 6.3 micromanipulator, which is driven by a stepper motor, a Kern PLE 310-3N precision balance and a Keithley 6400 source-meter. A self-written LabView program controls all components. To avoid any vibration damping the whole setup is located on a very rigid aluminum plate in a box filled with sand, which is mounted on a vibration isolated table. Stress-strain curves were measured by placing the sample in between the micromanipulator and the precision balance. For compression tests, the micromanipulator deforms the sample by a user defined step-size. After each step the program measures the force of the balance after a short settling time has been elapsed. These steps are repeated until the maximum deformation defined by the user is reached. Afterwards the direction of the deformation is inverted until the micromanipulator comes back to its original position. Finally, the stress-strain curves are evaluated and the Young's modulus is determined. With respect to the cyclic compression test, the same procedure was repeated several times. The wait time between each compression step was set to 0 s and the deformation speed was set to 40 μm/s. To demonstrate the structural integrity, a video during long-cycle compression test with an USB camera was recorded. Furthermore, the same setup also allows to record the current/voltage characteristics using the Keithley 6400 source-meter in the four-wire sense mode. For the electrical measurements the carbon structures were connected to thin copper plates on both sides

by using conductive silver paste. It is noteworthy that only a thin layer of paste was needed to ensure a good electrical connection of the porous material to the measurement setup. Current-voltage curves were measured in a voltage range of up to 5V. Finally, the resistance was calculated from the obtained data and converted to conductivity to give meaningful values for each structure.

4.3. Cell culture and cell seeding on scaffolds

Rat embryonic fibroblasts (REF52), both as wild type and stably transfected with YFP-paxillin (REF YFP-Pax)[69], were cultured in DMEM (Biochrom, Germany) at 37 °C, 5 % CO_2 at ~ 90 % humidity. The medium was supplemented with 10 % Fetal Bovine Serum (FBS; Biochrom, Germany) and 1 % penicillin/streptomycin (Sigma, Germany). In order to expel any traces of remaining zinc from the scaffold fabrication process prior to cell experiments, all samples were immersed in culture medium for 14 days after autoclaving at 121 °C. Shortly before the cell experiments, cells were immersed into fresh culture medium, counted with a cell counter (Scepter^{TM}, Merck Millipore, Germany) and ~ 20,000 cells were seeded on each scaffold in 24-well plates. Cells were incubated on the scaffolds for 1, 3 or 7 days.

4.4. Cell staining

To investigate cell morphology, proliferation and adhesion on the scaffolds, cell nuclei were stained with DAPI (ThermoFisher, Germany) and actin stress fibers were stained with Phalloidin (Alexa Fluor® 647 Phalloidin, ThermoFischer, Germany). Imaging was carried out using fluorescence microscopy (IX81, Olympus, Germany) and images were processed with cellSense Dimension (Olympus, Germany). For electron microscopy investigations, cells were fixed by

paraformaldehyde (ThermoFisher, Germany) and dried using critical point drying (EMS 3000). A thin layer of gold was sputtered (Bal-Tec SCD 050, 30mA, 30 sec) onto the sample prior to scanning electron microscopy (SEM) (Ultra Plus Zeiss SEM, 5 kV). The cells in SEM images were highlighted with green color (via Adobe Photoshop CC 2017) in order distinguish them more easily.

4.5. Viability and proliferation assay

The number of living cells on the scaffolds was quantified by a WST-1 proliferation assay after 1, 3 and 7 incubation days. In this assay, the number of living cells can be acquired from the amount of produced dye via bioreduction of stable tetrazolium salt WST-1 (Sigma-Aldrich, Germany). The amount of formazan is proportional to the number of cells (Cell Proliferation Reagent WST-1 Protocol, Sigma-Aldrich, Germany). The experiments were carried out as follows: After seeding the cells onto each sample (see specification above), the scaffolds were first washed with PBS and then incubated with a WST-1 containing medium for 4 hours. The concentration of the formazan dye was quantified by a multi-well spectrophotometer (Bio-Tek µQuant, USA) after removal of the samples from the wells. CNTs tend to react with tetrazolium salts[70], thus the proliferation rates were normalized to the absorption of the detected tetrazolium on control samples without cells. The amount of tetrazolium reacting with the scaffolds was determined for each sample as explained in the following: 10,000 cells were cultured for 24 hours in 96 well-plates prior to adding scaffolds to half of the wells, the other half serving as scaffold-free control. Then, all the wells were incubated for an additional time of 4 hours with the WST-1 reagent before quantification of the formazan (i.e. product of tetrazolium-cell reaction) amount in each well by the multi-well spectrophotometer. The amount of tetrazolium

that reacted with the scaffold was calculated for each specimen by subtracting the amount of formazan of scaffold-containing wells from scaffold-free control wells. The difference in absorbance between the scaffolds and controls was used as a correction factor for the data generated with the WST-1 assay.

In addition, the viability of cells was tested according to the ISO 10993 norm. Briefly, 10,000 cells/100 µl REF52 cells were cultured in a 96 well-plate for 24 hours. For medium extraction, the scaffolds were incubated in culture medium at 37°C for 72 hours. The cultured cells were either incubated with untreated medium or extracted medium for a further 24 hours. To determine cell viability, the colorimetric Methylthiazolyldiphenyl-tetrazolium bromide metabolic activity assay (MTT; Sigma-Aldrich, Germany) was used. The cells in untreated medium served as negative control and cells in 20 % DMSO were the positive control. The absorbance was measured at 490 nm (absorption wavelength of formazan) and 600 nm as a reference. The results from the cultured cells with extracted medium were normalized to the values measured for the negative control.

4.6. Protein adsorption rate

The protein adsorption rate on the scaffolds was measured by using bovine serum albumin (Pierce; ThermoFisher, Germany) as a model protein. 1 ml of protein solution (1 mg/ml) was added per scaffold and incubated at 37°C in a humidified incubator (CO_2 5 %, humidity 95 %). After 48 hours, non-adhered proteins were carefully removed by a pipette and saved for recording. The scaffolds were washed with saline and incubated for further 48 h after addition of 1 ml protein solution. The same procedure was repeated after 48 h. The concentration of protein in the supernatant was measured using a micro BCA protein assay (Pierce; ThermoFisher,

Germany). To do so, 10 µl of supernatant were mixed with 200 µl working reagent and incubated for 30 min. The absorbance was measured using a microplate reader (Bio-Tek µQuant, USA) at 570 nm. After calibrating the results with a standard curve provided by the BCA protein assay kit (Pierce; ThermoFisher, Germany), the protein adsorption rate was calculated by subtracting the residual protein concentration from the initial protein concentration.

ASSOCIATED CONTENT

Supporting Information.

The Supporting Information is available free of charge on the ACS Publications website at DOI: Supporting Information, containing Figures S1–S8 (PDF), supporting discussion, supporting movie

AUTHOR INFORMATION

Corresponding Author

* Email: cse@tf.uni-kiel.de

ACKNOWLEDGMENTS

RA gratefully acknowledges partial project funding by the Deutsche Forschungsgemeinschaft under contract FOR1616. This project has received funding from the European Union's Horizon 2020 research and innovation programme under grant agreement No. GrapheneCore2 785219. CS is supported by the European Research Council (ERC StG 336104 CELLINSPIRED, ERC PoC 768740 CHANNELMAT), by the German Research Foundation (RTG 2154, SFB 1261 project B7). MT acknowledges support from the German Academic Exchange Service (DAAD) through a research grant for doctoral candidates (91526555-57048249). We acknowledge funding from EPSRC grants EP/P02534X/1, ERC grant 319277 (Hetero2D) the Royal Academy of Engineering Enterprise Scheme, the Trinity College, Cambridge, and the Isaac Newton Trust. We also acknowledge Galen Ream for critical proofreading.

REFERENCES

(1) O'Brien, F. J. Biomaterials & Scaffolds for Tissue Engineering. *Mater. Today* **2011**, *14* (3), 88–95.

(2) Yang, S.; Leong, K.-F.; Du, Z.; Chua, C.-K. The Design of Scaffolds for Use in Tissue Engineering. Part I. Traditional Factors. *Tissue Eng.* **2001**, *7* (6), 679–689.

(3) Shoulders, M. D.; Raines, R. T. Collagen Structure and Stability. *Annu. Rev. Biochem.* **2009**, *78* (1), 929–958.

(4) Friedl, P.; Wolf, K. Plasticity of Cell Migration: A Multiscale Tuning Model. *J. Cell Biol.* **2010**, *188* (1), 11–19.

(5) Langer, R.; Vacanti, J. P. Tissue Engineering. *Science.* **1993**, *260* (5110), 920–926.

(6) Place, E. S.; Evans, N. D.; Stevens, M. M. Complexity in Biomaterials for Tissue Engineering. *Nat. Mater.* **2009**, *8* (6), 457–470.

(7) Loh, Q. L.; Choong, C. Three-Dimensional Scaffolds for Tissue Engineering Applications: Role of Porosity and Pore Size. *Tissue Eng. Part B Rev.* **2013**, *19* (6), 485–502.

(8) Ganji, Y.; Li, Q.; Quabius, E. S.; Böttner, M.; Selhuber-Unkel, C.; Kasra, M. Cardiomyocyte Behavior on Biodegradable Polyurethane/Gold Nanocomposite Scaffolds under Electrical Stimulation. *Mater. Sci. Eng. C* **2016**, *59*, 10–18.

(9) Potse, M.; Dubé, B.; Vinet, A. Cardiac Anisotropy in Boundary-Element Models for the Electrocardiogram. *Med. Biol. Eng. Comput.* **2009**, *47* (7), 719–729.

(10) Fang, B.; Yang, J.; Chen, C.; Zhang, C.; Chang, D.; Xu, H.; Gao, C. Carbon Nanotubes Loaded on Graphene Microfolds as Efficient Bifunctional Electrocatalysts for the Oxygen Reduction and Oxygen Evolution Reactions. *ChemCatChem* **2017**, *9* (24), 4520–4528.

(11) Li, Z.; Liu, Z.; Sun, H.; Gao, C. Superstructured Assembly of Nanocarbons: Fullerenes, Nanotubes, and Graphene. *Chem. Rev.* **2015**, *115* (15), 7046–7117.

(12) Lekawa-Raus, A.; Patmore, J.; Kurzepa, L.; Bulmer, J.; Koziol, K. Electrical Properties of Carbon Nanotube Based Fibers and Their Future Use in Electrical Wiring. *Adv. Funct. Mater.* **2014**, *24* (24), 3661–3682.

(13) Sahebian, S.; Zebarjad, S. M.; vahdati Khaki, J.; Lazzeri, A. A Study on the Dependence of Structure of Multi-Walled Carbon Nanotubes on Acid Treatment. *J. Nanostructure Chem.* **2015**, *5* (3), 287–293.

(14) Aliofkhazraei, M.; Ali, N.; Milne, W. I.; Ozkan, C. S.; Mitura, S.; Gervasoni, J. L. Graphene Science Handbook: Electrical and Optical Properties; CRC Press, 2016; p 715.

(15) Chen, J. H.; Jang, C.; Xiao, S.; Ishigami, M.; Fuhrer, M. S. Intrinsic and Extrinsic Performance Limits of Graphene Devices on SiO2. *Nat. Nanotechnol.* **2008**, *3* (4), 206–209.

(16) Gorityala, B. K.; Ma, J.; Wang, X.; Chen, P.; Liu, X. W. Carbohydrate Functionalized Carbon Nanotubes and Their Applications. *Chem. Soc. Rev.* **2010**, *39* (8), 2925–2934.

(17) Bhunia, S. K.; Saha, A.; Maity, A. R.; Ray, S. C.; Jana, N. R. Carbon Nanoparticle-Based Fluorescent Bioimaging Probes. *Sci. Rep.* **2013**, *3* (1), 1473.

(18) Fabbro, A.; Scaini, D.; León, V.; Vázquez, E.; Cellot, G.; Privitera, G.; Lombardi, L.; Torrisi, F.; Tomarchio, F.; Bonaccorso, F.; F.; Bosi, S.; Ferrari, A. C.; Ballerini, L.; Prato, M. Graphene-Based Interfaces Do Not Alter Target Nerve Cells. *ACS Nano* **2016**, *10* (1), 615–623.

(19) Call, T. P.; Carey, T.; Bombelli, P.; Lea-Smith, D. J.; Hooper, P.; Howe, C. J.; Torrisi, F. Platinum-Free, Graphene Based Anodes and Air Cathodes for Single Chamber Microbial Fuel Cells. *J. Mater. Chem. A* **2017**, *5* (45), 23872–23886.

(20) Li, N.; Zhang, Q.; Gao, S.; Song, Q.; Huang, R.; Wang, L.; Liu, L.; Dai, J.; Tang, M.; Cheng, G. Three-Dimensional Graphene Foam as a Biocompatible and Conductive Scaffold for Neural Stem Cells. *Sci. Rep.* **2013**, *3*, 1604.

(21) Mooney, E.; Dockery, P.; Greiser, U.; Murphy, M.; Barron, V. Carbon Nanotubes and

Mesenchymal Stem Cells: Biocompatibility, Proliferation and Differentiation. *Nano Lett.* **2008**, *8* (8), 2137–2143.

(22) Yang, S. T.; Luo, J.; Zhou, Q.; Wang, H. Pharmacokinetics, Metabolism and Toxicity of Carbon Nanotubes for Bio-Medical Purposes. *Theranostics* **2012**, *2* (3), 271–282.

(23) Jia, G.; Wang, H.; Yan, L.; Wang, X.; Pei, R.; Yan, T.; Zhao, Y.; Guo, X. Cytotoxicity of Carbon Nanomaterials: Single-Wall Nanotube, Multi-Wall Nanotube, and Fullerene. *Environ. Sci. Technol.* **2005**, *39* (5), 1378–1383.

(24) M A Correa-Duarte, N Wagner, J Rojas-Chapana, C Morsczeck, M Thie, M. G. Fabrication and Biocompatibilut of Carbon Nanobute-Based 3D Networks as Scaffolds for Cell Seeding and Growth. *Nano Lett.* **2004**, *4* (11), 2233–2236.

(25) Edwards, S. L.; Church, J. S.; Werkmeister, J. A.; Ramshaw, J. A. M. Tubular Micro-Scale Multiwalled Carbon Nanotube-Based Scaffolds for Tissue Engineering. *Biomaterials* **2009**, *30* (9), 1725–1731.

(26) Liu, Y.; Zhao, Y.; Sun, B.; Chen, C. Understanding the Toxicity of Carbon Nanotubes. *Acc. Chem. Res.* **2013**, *46* (3), 702–713.

(27) Cohen-Karni, T.; Qing, Q.; Li, Q.; Fang, Y.; Lieber, C. M. Graphene and Nanowire Transistors for Cellular Interfaces and Electrical Recording. *Nano Lett.* **2010**, *10* (3), 1098–1102.

(28) Akhavan, O.; Ghaderi, E.; Shahsavar, M. Graphene Nanogrids for Selective and Fast Osteogenic Differentiation of Human Mesenchymal Stem Cells. *Carbon* **2013**, *59*, 200–211.

(29) Shin, S. R.; Li, Y. C.; Jang, H. L.; Khoshakhlagh, P.; Akbari, M.; Nasajpour, A.; Zhang, Y. S.; Tamayol, A.; Khademhosseini, A. Graphene-Based Materials for Tissue Engineering. *Adv. Drug Deliv. Rev.* **2016**, *105*, 255–274.

(30) Smith, S. C.; Ahmed, F.; Gutierrez, K. M.; Frigi Rodrigues, D. A Comparative Study of Lysozyme Adsorption with Graphene, Graphene Oxide, and Single-Walled Carbon

Nanotubes: Potential Environmental Applications. *Chem. Eng. J.* **2014**, *240*, 147–154.

(31) Mecklenburg, M.; Schuchardt, A.; Mishra, Y. K.; Kaps, S.; Adelung, R.; Lotnyk, A.; Kienle, L.; Schulte, K. Aerographite: Ultra Lightweight, Flexible Nanowall, Carbon Microtube Material with Outstanding Mechanical Performance. *Adv. Mater.* **2012**, *24* (26), 3486–3490.

(32) Mishra, Y. K.; Kaps, S.; Schuchardt, A.; Paulowicz, I.; Jin, X.; Gedamu, D.; Freitag, S.; Claus, M.; Wille, S.; Kovalev, A.; Gorb, S. N.; Adelung, R. Fabrication of Macroscopically Flexible and Highly Porous 3D Semiconductor Networks from Interpenetrating Nanostructures by a Simple Flame Transport Approach. *Part. Part. Syst. Charact.* **2013**, *30* (9), 775–783.

(33) Lamprecht, C.; Taale, M.; Paulowicz, I.; Westerhaus, H.; Grabosch, C.; Schuchardt, A.; Mecklenburg, M.; Böttner, M.; Lucius, R.; Schulte, K.; Adelung, R.; Selhuber-Unkel, C. A Tunable Scaffold of Microtubular Graphite for 3D Cell Growth. *ACS Appl. Mater. Interfaces* **2016**, *8* (24), 14980–14985, DOI: 10.1021/acsami.6b00778.

(34) Mouw, J. K.; Ou, G.; Weaver, V. M. Extracellular Matrix Assembly: A Multiscale Deconstruction. *Nat. Rev. Mol. Cell Biol.* **2014**, *15* (12), 771–785.

(35) Schütt, F.; Signetti, S.; Krüger, H.; Röder, S.; Smazna, D.; Kaps, S.; Gorb, S. N.; Mishra, Y. K.; Pugno, N. M.; Adelung, R. Hierarchical Self-Entangled Carbon Nanotube Tube Networks. *Nat. Commun.* **2017**, *8* (1), DOI: 10.1038/s41467-017-01324-7.

(36) Feng, X.; Feng, L.; Jin, M.; Zhai, J.; Jiang, L.; Zhu, D. Reversible Super-Hydrophobicity to Super-Hydrophilicity Transition of Aligned ZnO Nanorod Films. *J. Am. Chem. Soc.* **2004**, *126* (1), 62–63.

(37) Chen, H.-K. Kinetic Study on the Carbothermic Reduction of Zinc Oxide. *Scand. J. Metall.* **2001**, *30* (5), 292–296.

(38) Zhao, J.; Xing, B.; Yang, H.; Pan, Q.; Li, Z.; Liu, Z. Growth of Carbon Nanotubes on Graphene by Chemical Vapor Deposition. *New Carbon Mater.* **2016**, *31* (1), 31–36.

(39) Ferrari, A. C.; Robertson, J. Resonant Raman Spectroscopy of Disordered, Amorphous, and Diamondlike Carbon. *Phys. Rev. B - Condens. Matter Mater. Phys.* **2001**, *64* (7).

(40) Carey, T.; Cacovich, S.; Divitini, G.; Ren, J.; Mansouri, A.; Kim, J. M.; Wang, C.; Ducati, C.; Sordan, R.; Torrisi, F. Fully Inkjet-Printed Two-Dimensional Material Field-Effect Heterojunctions for Wearable and Textile Electronics. *Nat. Commun.* **2017**, *8* (1), 1202.

(41) Ferrari, A. C.; Meyer, J. C.; Scardaci, V.; Casiraghi, C.; Lazzeri, M.; Mauri, F.; Piscanec, S.; Jiang, D.; Novoselov, K. S.; Roth, S.; et al. Raman Spectrum of Graphene and Graphene Layers. *Phys. Rev. Lett.* **2006**, *97* (18).

(42) Ferrari, A.; Robertson, J. Interpretation of Raman Spectra of Disordered and Amorphous Carbon. *Phys. Rev. B - Condens. Matter Mater. Phys.* **2000**, *61* (20), 14095–14107.

(43) Cuscó, R.; Alarcón-Lladó, E.; Ibáñez, J.; Artús, L.; Jiménez, J.; Wang, B.; Callahan, M. Temperature Dependence of Raman Scattering in ZnO. *Phys. Rev. B* **2007**, *75* (16), 1–11.

(44) Fan, H.; Wang, L.; Zhao, K.; Li, N.; Shi, Z.; Ge, Z.; Jin, Z. Fabrication, Mechanical Properties, and Biocompatibility of Graphene-Reinforced Chitosan Composites. *Biomacromolecules* **2010**, *11* (9), 2345–2351.

(45) Ahadian, S.; Ramón-Azcón, J.; Estili, M.; Liang, X.; Ostrovidov, S.; Shiku, H.; Ramalingam, M.; Nakajima, K.; Sakka, Y.; Bae, H.; H.; Matsue, T.; Khademhosseini, A. Hybrid Hydrogels Containing Vertically Aligned Carbon Nanotubes with Anisotropic Electrical Conductivity for Muscle Myofiber Fabrication. *Sci. Rep.* **2014**, *4* (1), 4271.

(46) Shi, X.; Sitharaman, B.; Pham, Q. P.; Liang, F.; Wu, K.; Edward Billups, W.; Wilson, L. J.; Mikos, A. G. Fabrication of Porous Ultra-Short Single-Walled Carbon Nanotube Nanocomposite Scaffolds for Bone Tissue Engineering. *Biomaterials* **2007**, *28* (28), 4078–4090.

(47) Chen, Z.; Ren, W.; Gao, L.; Liu, B.; Pei, S.; Cheng, H. M. Three-Dimensional Flexible and Conductive Interconnected Graphene Networks Grown by Chemical Vapour Deposition. *Nat. Mater.* **2011**, *10* (6), 424–428.

(48) Zhao, G.; Zhang, X.; Lu, T. J.; Xu, F. Recent Advances in Electrospun Nanofibrous Scaffolds for Cardiac Tissue Engineering. *Adv. Funct. Mater.* **2015**, *25* (36), 5726–5738.

(49) Zuo, G.; Kang, S. G.; Xiu, P.; Zhao, Y.; Zhou, R. Interactions between Proteins and Carbon-Based Nanoparticles: Exploring the Origin of Nanotoxicity at the Molecular Level. *Small* **2013**, *9* (9–10), 1546–1556.

(50) Suh, C. W.; Kim, M. Y.; Choo, J. B.; Kim, J. K.; Kim, H. K.; Lee, E. K. Analysis of Protein Adsorption Characteristics to Nano-Pore Silica Particles by Using Confocal Laser Scanning Microscopy. *J. Biotechnol.* **2004**, *112* (3), 267–277.

(51) Prager-Khoutorsky, M.; Lichtenstein, A.; Krishnan, R.; Rajendran, K.; Mayo, A.; Kam, Z.; Geiger, B.; Bershadsky, A. D. Fibroblast Polarization Is a Matrix-Rigidity-Dependent Process Controlled by Focal Adhesion Mechanosensing. *Nat. Cell Biol.* **2011**, *13* (12), 1457–1465.

(52) El-Mohri, H.; Wu, Y.; Mohanty, S.; Ghosh, G. Impact of Matrix Stiffness on Fibroblast Function. *Mater. Sci. Eng. C* **2017**, *74*, 146–151.

(53) Sun, Y.; Chen, C. S.; Fu, J. Forcing Stem Cells to Behave: A Biophysical Perspective of the Cellular Microenvironment. *Annu. Rev. Biophys.* **2012**, *41* (1), 519–542.

(54) Moreno-Arotzena, O.; Borau, C.; Movilla, N.; Vicente-Manzanares, M.; García-Aznar, J. M. Fibroblast Migration in 3D Is Controlled by Haptotaxis in a Non-Muscle Myosin II-Dependent Manner. *Ann. Biomed. Eng.* **2015**, *43* (12), 3025–3039.

(55) Turner, C. E. Paxillin and Focal Adhesion Signalling. *Nat. Cell Biol.* **2000**, *2* (12), E231–E236.

(56) Chiu, C.-L.; Aguilar, J. S.; Tsai, C. Y.; Wu, G.; Gratton, E.; Digman, M. M. A.; Kuo, J.; Han, X.; Hsiao, C.; Iii, J. Y.; et al. Nanoimaging of Focal Adhesion Dynamics in 3D. *PLoS One* **2014**, *9* (6), e99896.

(57) Ryoo, S. R.; Kim, Y. K.; Kim, M. H.; Min, D. H. Behaviors of NIH-3T3 Fibroblasts on Graphene/Carbon Nanotubes: Proliferation, Focal Adhesion, and Gene Transfection

Studies. *ACS Nano* **2010**, *4* (11), 6587–6598.

(58) Cooper, G. M. *The Cell: A Molecular Approach*; ASM Press, 2000; Vol. 10.

(59) Serrano, M. C.; Patiño, J.; García-Rama, C.; Ferrer, M. L.; Fierro, J. L. G.; Tamayo, A.; Collazos-Castro, J. E.; Del Monte, F.; Gutiérrez, M. C. 3D Free-Standing Porous Scaffolds Made of Graphene Oxide as Substrates for Neural Cell Growth. *J. Mater. Chem. B* **2014**, *2* (34), 5698–5706.

(60) Avery, N. C.; Bailey, A. J.; Fratzl, P. *Collagen: Structure and Mechanics*; Springer, 2008.

(61) LeBaron, R. G.; Athanasiou, K. A. Extracellular Matrix Cell Adhesion Peptides: Functional Applications in Orthopedic Materials. *Tissue Eng.* **2000**, *6* (2), 85–103.

(62) Marx, J.; Lewke, M. R. D.; Smazna, D.; Mishra, Y. K.; Adelung, R.; Schulte, K.; Fiedler, B. Processing, Growth Mechanism and Thermodynamic Calculations of Carbon Foam with a Hollow Tetrapodal Morphology – Aerographite. *Appl. Surf. Sci.* **2019**, *470*, 535–542.

(63) Wang, F.; Torrisi, F.; Jiang, Z.; Popa, D.; Hasan, T.; Sun, Z.; Cho, W.; Ferrari, A. C. Graphene Passively Q-Switched Two-Micron Fiber Lasers. *Conf. Lasers Electro-Optics 2012* **2012**, JW2A.72.

(64) Purdie, D. G.; Popa, D.; Wittwer, V. J.; Jiang, Z.; Bonacchini, G.; Torrisi, F.; Milana, S.; Lidorikis, E.; Ferrari, A. C. Few-Cycle Pulses from a Graphene Mode-Locked All-Fiber Laser. *Appl. Phys. Lett.* **2015**, *106* (25), 253101.

(65) Bianchi, V.; Carey, T.; Viti, L.; Li, L.; Linfield, E. H.; Davies, A. G.; Tredicucci, A.; Yoon, D.; Karagiannidis, P. G.; Lombardi, L.; Tomarchio, F.; Ferrari, A. C.; Torrisi, F.; Vitiello, M. S. Terahertz Saturable Absorbers from Liquid Phase Exfoliation of Graphite. *Nat. Commun.* **2017**, *8*, 15763.

(66) Lotya, M.; Hernandez, Y.; King, P. J.; Smith, R. J.; Nicolosi, V.; Karlsson, L. S.; Blighe, F. M.; De, S.; Zhiming, W.; McGovern, I. T.; Duesberg, G. S.; Coleman, J. N. Liquid Phase Production of Graphene by Exfoliation of Graphite in Surfactant/Water Solutions.

J. Am. Chem. Soc. **2009**, *131* (10), 3611–3620.

(67) Carey, T.; Jones, C.; Le Moal, F.; Deganello, D.; Torrisi, F. Spray Coating Thin Films on Three-Dimensional Surfaces for a Semi-Transparent Capacitive Touch Device. *ACS Appl. Mater. Interfaces* **2018**, *10* (23), 19948–19956.

(68) Kravets, V. G.; Grigorenko, A. N.; Nair, R. R.; Blake, P.; Anissimova, S.; Novoselov, K. S.; Geim, A. K. Spectroscopic Ellipsometry of Graphene and an Exciton-Shifted van Hove Peak in Absorption. *Phys. Rev. B - Condens. Matter Mater. Phys.* **2010**, *81* (15), 155413.

(69) Selhuber-Unkel, C.; Erdmann, T.; López-García, M.; Kessler, H.; Schwarz, U. S.; Spatz, J. P. Cell Adhesion Strength Is Controlled by Intermolecular Spacing of Adhesion Receptors. *Biophys. J.* **2010**, *98* (4), 543–551.

(70) Wörle-Knirsch, J. M.; Pulskamp, K.; Krug, H. F. Oops They Did It Again! Carbon Nanotubes Hoax Scientists in Viability Assays. *Nano Lett.* **2006**, *6* (6), 1261–1268.

Table of Content Image